



TITLE:

# Hydrogen-related Fatigue Fracture under Various Test Frequencies in Low-carbon Martensitic Steel

AUTHOR(S):

Matsumiya, Hisashi; Shibata, Akinobu; Maegawa, Yoshiaki; Okada, Kazuho; Tsuji, Nobuhiro

---

CITATION:

Matsumiya, Hisashi ...[et al]. Hydrogen-related Fatigue Fracture under Various Test Frequencies in Low-carbon Martensitic Steel. ISIJ International 2022, 62(10): 2089-2094

ISSUE DATE:

2022-10-15



URL:

<http://hdl.handle.net/2433/279065>

RIGHT:

© 2022 The Iron and Steel Institute of Japan.; This is an open access article under the terms of the Creative Commons Attribution-NonCommercial-NoDerivs license.

# Hydrogen-related Fatigue Fracture under Various Test Frequencies in Low-carbon Martensitic Steel

Hisashi MATSUMIYA,<sup>1)\*</sup> Akinobu SHIBATA,<sup>2,3)</sup>  Yoshiaki MAEGAWA,<sup>1)</sup> Kazuho OKADA<sup>1,2)</sup> and Nobuhiro TSUJI<sup>1,3)</sup> 

- 1) Department of Materials Science and Engineering, Kyoto University, Yoshida-honmachi, Sakyo-ku, Kyoto, 606-8501 Japan.  
2) Research Center for Structural Materials, National Institute for Materials Science (NIMS), 1-2-1 Sengen, Tsukuba, 305-0047 Japan.  
3) Elements Strategy Initiative for Structural Materials (ESISM), Kyoto University, Yoshida-honmachi, Sakyo-ku, Kyoto, 606-8501 Japan.

(Received on April 29, 2022; accepted on June 15, 2022; J-STAGE Advance published date: July 6, 2022)

The present study investigated the hydrogen-related fatigue fracture under various test frequencies in low-carbon martensitic steel. In the hydrogen-charged specimen, although the number of cycles to failure decreased with decreasing test frequency, the time to failure was almost the same regardless of the test frequency. Observation of fracture surface revealed that the transgranular surface was a main component in the uncharged specimen, while the intergranular surface was often observed especially at the lower test frequency in the hydrogen-charged specimen. In addition, for the transgranular fracture, cracks often propagated across the laths regardless of test conditions. The high-strained region was observed over a relatively wide area in the uncharged specimen. On the other hand, the hydrogen-related fatigue-crack propagation was accompanied by intense localized plastic deformation, which could accelerate crack growth. The intergranular cracking and high localization of plastic deformation could be the possible reasons for decreasing the fatigue life by the presence of hydrogen.

KEY WORDS: hydrogen embrittlement; fatigue fracture; test frequency; martensitic steel; electron back-scattering diffraction; crystallographic orientation analysis.

## 1. Introduction

Owing to improvement of fuel-efficiency and collision safety, the demand of high-strength steels such as martensitic steels is increasing. Low-carbon martensitic steels often exhibit a lath martensite structure, which is composed of several different length-scale units; laths, blocks, and packets existing inside one prior austenite grain.<sup>1–4)</sup> A lath is a single crystal of martensite with a thickness of approximately 0.2  $\mu\text{m}$ . A block consists of several laths with nearly the same crystallographic orientation. A packet is an aggregation of laths (or blocks) with nearly the identical habit plane. It has been reported that mechanical properties of martensitic steels are affected by such a complicated microstructure.<sup>5–8)</sup>

High-strength martensitic steels are sometimes subjected to alternating loading circumstances, which may cause serious accidents by fatigue fracture. Hence, preventing fatigue fracture of martensitic steels is recognized as an important

technological challenge. Recently, several researches focusing on relationship between fatigue property and microstructure of martensitic steels have been reported. Okada *et al.*<sup>9)</sup> conducted crystallographic analysis on fatigue crack initiation of low-carbon martensitic steel, and clearly showed that incompatibility of plastic strains between adjacent blocks was the origin for the formation of initial fatigue cracks at block boundaries. Ueki *et al.*<sup>10–12)</sup> performed crystallographic analysis on fatigue crack propagation in low-carbon martensitic steels using miniaturized compact-tension specimens. They proposed that the orientation relationship between the longitudinal directions of the martensite laths and the slip direction dominated the fatigue crack growth resistance.

It is also well known that hydrogen enhances fatigue crack growth.<sup>13–19)</sup> For understanding fatigue-cracking behavior in hydrogen environment, it is also necessary to clarify the relationship between cracking behavior and microstructure of martensitic steels. We previously performed fractographic analysis and found that fatigue crack initiated on prior austenite grain boundary in hydrogen environment

\* Corresponding author: E-mail: [matsumiya.hisashi.42a@st.kyoto-u.ac.jp](mailto:matsumiya.hisashi.42a@st.kyoto-u.ac.jp)



and propagated in transgranular manner.<sup>20)</sup> In addition to microstructure, the test condition also has a large influence on hydrogen-related fatigue property. Matsunaga *et al.* reported that the rate of fatigue crack growth accelerated by hydrogen gradually increased with a decrease in the test frequency.<sup>21)</sup> However, the underlying mechanism of hydrogen-assisted fatigue propagation behavior depending on the test frequency has yet to be fully understood. In this study, tension-tension fatigue tests were performed on hydrogen-charged as-quenched martensitic steel at test frequencies of 0.1 Hz, 1 Hz and 10 Hz, and the hydrogen-assisted fatigue fracture behavior was analyzed through microstructural and crystallographic analysis.

## 2. Experimental

The present study used a 2Mn-0.1C (mass%) steel. The detailed chemical composition of the steel is C: 0.103, Si: 0.01, Mn: 2.03, P: <0.002, S: 0.0010, Fe: bal. (mass%). As-cast ingot of the steel was cold-rolled from 15 mm to 1.5 mm in thickness. Then, the specimens were austenitized at 900°C for 1.8 ks in vacuum and quenched in iced-brine bath. After the heat treatment, both sides of the specimens were mechanically ground down to a thickness of 1 mm in order to remove the decarburized layers formed during the heat treatment.

Sheet type tensile/fatigue test specimens with a gauge length of 10 mm, width of 5 mm, and thickness of 1 mm were prepared from the heat-treated specimens. The tensile/fatigue test specimens were polished electrolytically in a solution of 50 ml HClO<sub>4</sub> + 450 ml CH<sub>3</sub>COOH, and cathodically pre-charged with hydrogen for 24 h at a current density of 5 A m<sup>-2</sup>. The hydrogen charging solution was an aqueous solution of 3% NaCl + 3 g L<sup>-1</sup> NH<sub>4</sub>SCN. A platinum wire was used as the counter electrode. The hydrogen content measured by thermal desorption spectrometry (R-DEC: HTDS-002) analysis was 0.943 wt. ppm.

Stress-controlled tensile-tensile fatigue tests were carried out using a servo-hydraulic machine (Shimazu, SERVO EHF-EV101k1) with a nominal stress range from 200 to 1 000 MPa. The employed stress ratio was 0, and the stress waveform was a sinusoidal wave. The test frequency was changed from 0.1 to 10 Hz. Uniaxial tensile tests at an initial strain rate of 8.3 × 10<sup>-6</sup> s<sup>-1</sup> were also conducted. The fatigue tests and tensile tests were performed at ambient temperature in air or under hydrogen concurrent-charging condition. For the tests under hydrogen concurrent-charging, the charging conditions were the same as that in the pre-charging procedure described above.

Microstructures and fracture surfaces of the fatigue-tested specimens were observed by optical microscopy and scanning electron microscopy (SEM, JEOL: JSM-7800F). Crystal orientation mappings were performed using electron backscattering diffraction (EBSD) in SEM (JEOL: JSM-7100F) at an acceleration voltage of 15 kV and a working distance of 15 mm. EBSD step sizes of 20 and 200 nm were used. The fracture surfaces were preserved by electrodeposition of Ni layer (thickness was approximately 100 μm). The electrodeposition solution was an aqueous solution of 150 g L<sup>-1</sup> Ni<sub>2</sub>SO<sub>4</sub> + 15 g L<sup>-1</sup> H<sub>3</sub>BO<sub>4</sub>. The Ni deposition was conducted at ambient temperature and at a current

density of 30 A m<sup>-2</sup> for 3 days. One side of the Ni electrodeposited specimen was mechanically polished and electrolytically polished in the same solution as described above. Finally, vibration polishing using a 0.02 μm colloidal silica suspension was conducted in order to remove roughness of the observation section. The EBSD orientation analysis was performed on the mid-cross sections perpendicular to the normal direction of the tested specimens.

## 3. Results

**Figure 1** shows an optical microscopy image of the heat-treated specimen. A typical lath martensite structure composed of several blocks and packets inside each prior austenite grain was observed, and no pro-eutectoid ferrite was confirmed. The mean prior austenite grain size was 47.7 μm. The nominal stress – nominal strain curves of the uncharged and hydrogen-charged specimens were shown in **Fig. 2**. The 0.2% proof stress and tensile strength of the uncharged specimen were 849 MPa and 1 177 MPa, respectively. The total elongation of the hydrogen-charged specimen was 1.5%, and significantly limited compared with that of the uncharged specimen (11.3%).

**Figure 3** presents (a) the relationship between stress

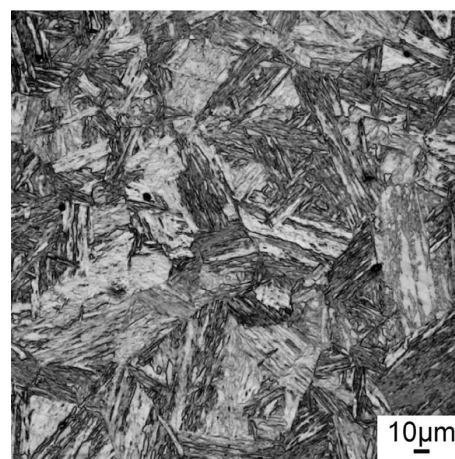


**Fig. 1.** Optical microscopy image of the heat-treated specimen.

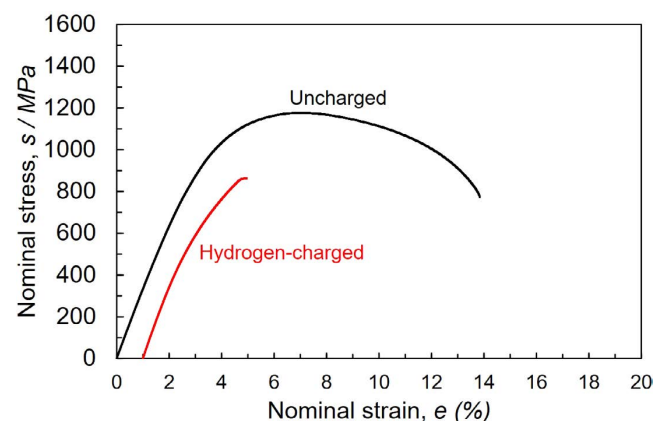


**Fig. 2.** Nominal stress – nominal strain curves of the uncharged specimen (black line) and hydrogen-charged specimen (red line). The data from previous study<sup>20)</sup> was reused here (reproduced with permission from Elsevier). (Online version in color.)

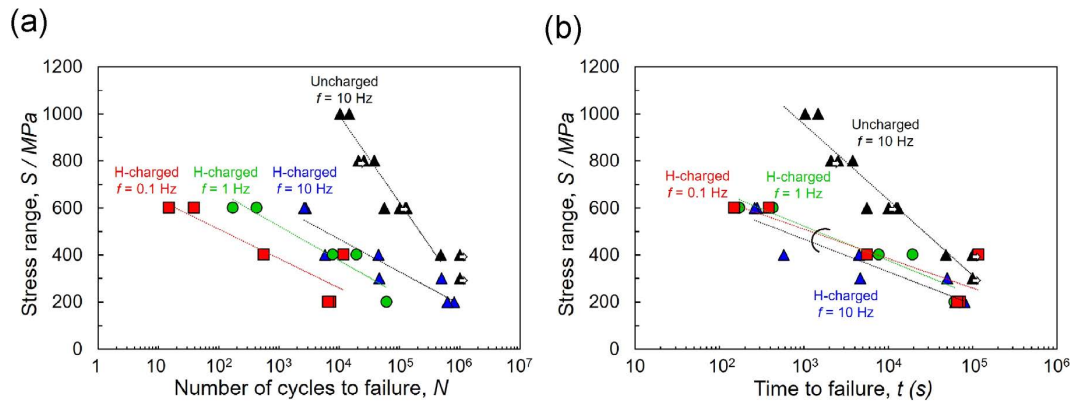


**Fig. 3.** (a)  $S$ - $N$  plots and (b) relationship between stress range and time to failure of the uncharged specimen tested at  $f = 10$  Hz (black triangles) and the hydrogen-charged specimens tested at  $f = 10$  Hz (blue triangles), 1 Hz (green circles), and 0.1 Hz (red squares). The white arrows indicate that the tests were stopped before final rupture. (Online version in color.)

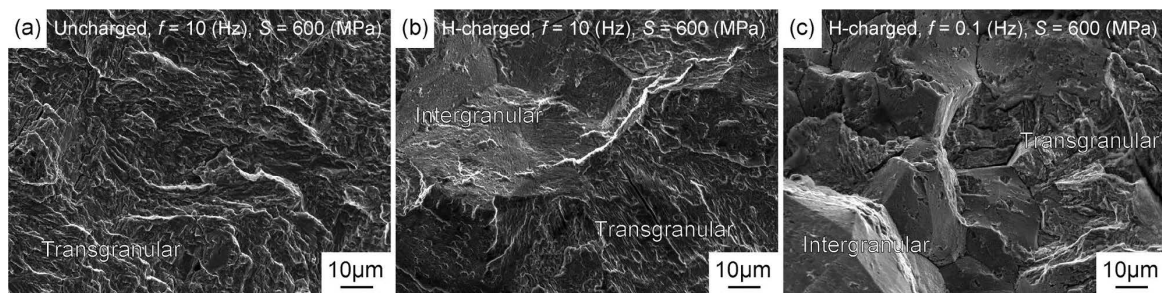


**Fig. 4.** SEM images showing the fracture surfaces of the (a) uncharged specimen tested at  $f = 10$  Hz and  $S = 600$  MPa, (b) hydrogen-charged specimen tested at  $f = 10$  Hz and  $S = 600$  MPa, and (c) hydrogen-charged specimen tested at  $f = 0.1$  Hz and  $S = 600$  MPa.

range and number of cycles to failure ( $S$ - $N$  plots) and (b) the relationship between stress range and time to failure of the uncharged specimen (black triangle) and hydrogen-charged specimens (red rectangle:  $f = 0.1$  Hz, green circle:  $f = 1$  Hz, and blue triangle:  $f = 10$  Hz). As shown in Fig. 3(a), the number of cycles to failure in the hydrogen-charged specimen was much smaller than that in the uncharged specimen, and significantly decreased with decreasing test frequency. Although the test frequency affected the fatigue life in the hydrogen-charged specimen, the time to failure was almost the same regardless of the test frequency as shown in Fig. 3(b).

**Figure 4** shows the fracture surfaces of the (a) uncharged specimen at  $f = 10$  Hz, and (b) and (c) hydrogen-charged specimens at  $f = 10$  Hz and 0.1 Hz, respectively. The fracture surface of the uncharged specimen mainly comprised transgranular surface. On the other hand, intergranular surface in addition to transgranular surface was observed in the hydrogen-charged specimen, as shown in Figs. 4(b) and 4(c). Moreover, the intergranular surface was frequently observed at  $f = 0.1$  Hz (Fig. 4(c)). **Figure 5** summarizes the area fraction of intergranular surface in the region other than dimples. We can find that the area fraction of intergranular surface in the hydrogen-charged specimen was much higher, particularly at the lower stress range and lower test frequency, than that in the uncharged specimen.

**Figure 6** shows (a), (b), (d), (e), (g) and (h) SEM images, and (c), (f) and (i) EBSD orientation maps around the fatigue cracks of the (a)–(c) uncharged specimen at  $f =$

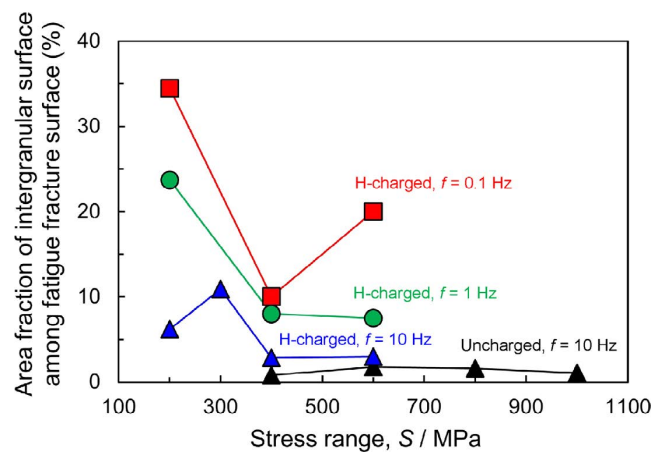


**Fig. 5.** Area fraction of intergranular surface among fatigue fracture surface (*i.e.*, other than dimples). The black, blue, green, and red plots correspond to the uncharged specimens tested at  $f = 10$  Hz, the hydrogen-charged specimens tested at  $f = 10$  Hz, the hydrogen-charged specimens tested at  $f = 1$  Hz, and the hydrogen-charged specimens tested at  $f = 0.1$  Hz, respectively. (Online version in color.)

10 Hz, (d)–(f) hydrogen-charged specimen at  $f = 10$  Hz, and (g)–(i) hydrogen-charged specimen at  $f = 0.1$  Hz. The observation areas of (b, c), (e, f), and (h, i) are indicated in (a), (d), and (g), respectively. As shown in Fig. 6(c), (f), the fatigue cracks propagated across the laths or parallel to the block boundaries (but inside the block) in the uncharged and hydrogen-charged specimens at  $f = 10$  Hz.

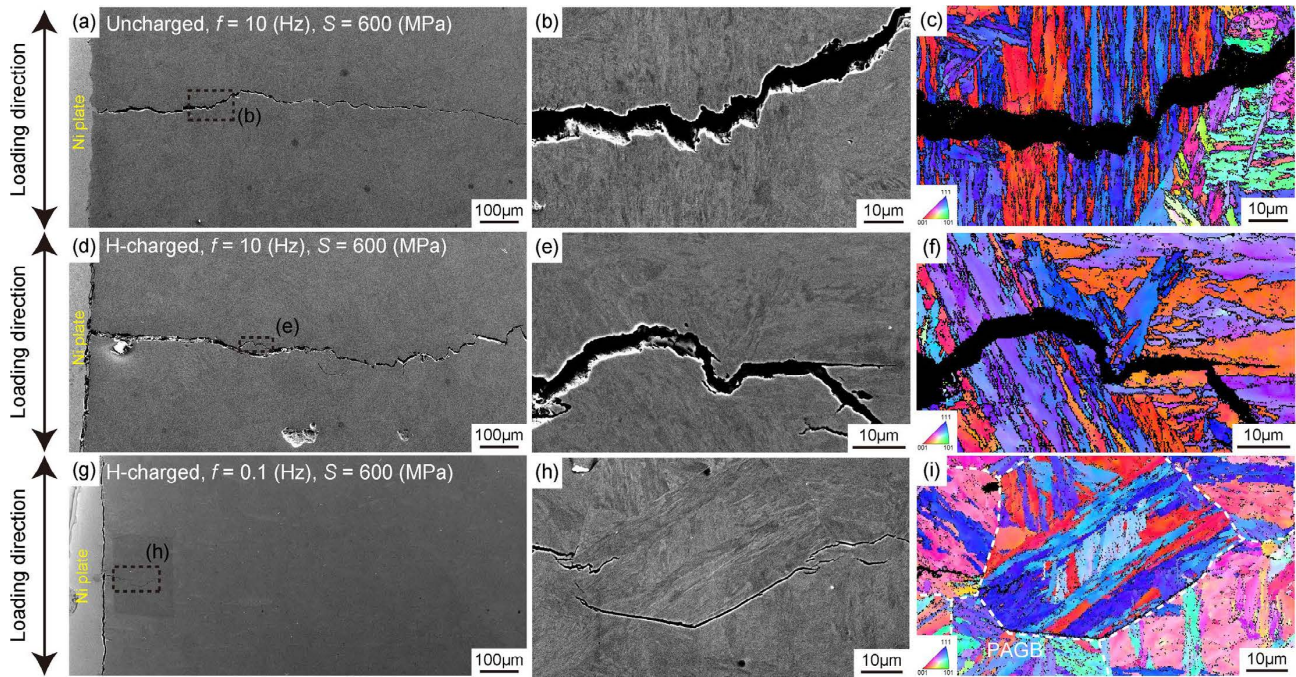


**Fig. 6.** (a), (b), (d), (e), (g) and (h) SEM images and (c), (f) and (i) EBSD-orientation maps showing the areas around the cracks: (a)–(c) the uncharged specimen tested at  $f = 10$  Hz, (d)–(f) the hydrogen-charged specimen tested at  $f = 10$  Hz, (g)–(i) the hydrogen-charged specimen tested at  $f = 0.1$  Hz. The positions of the prior austenite grain boundaries determined by EBSD orientation analysis are indicated in (i) by the white broken lines. (Online version in color.)

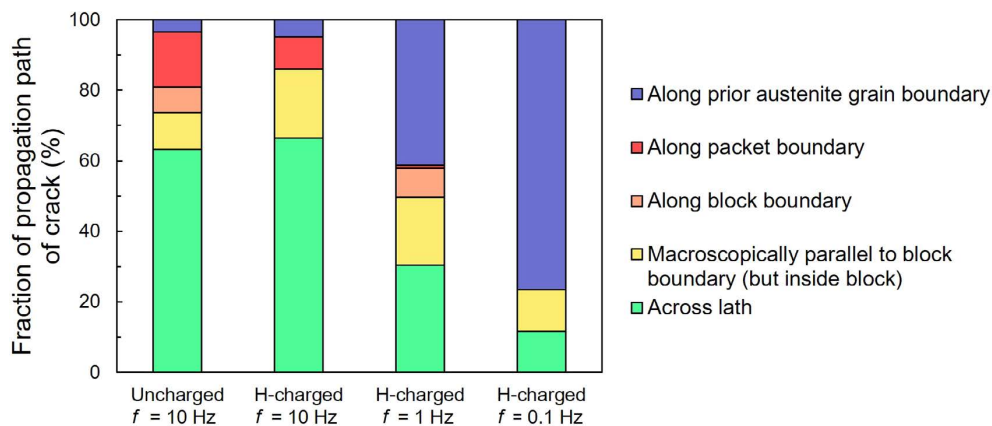


**Fig. 7.** Fraction of propagation path of crack existing in the area within  $200 \mu\text{m}$  from the crack initiation site; across lath, macroscopically parallel to block boundary (but inside block), along block boundary, along packet boundary, and along prior austenite grain boundary are indicated in green, yellow, orange, red and blue, respectively. (Online version in color.)

This indicates that hydrogen did not significantly change the crack path when tested at the higher test frequency. In contrast, the crack mainly propagated along prior austenite grain boundaries (indicated by white broken lines) in the hydrogen-charged specimen at  $f = 0.1$  Hz as shown in Fig. 6(i). The propagation path of the cracks existing in the area within  $200 \mu\text{m}$  from the crack initiation sites was quantitatively analyzed and results are summarized in Fig. 7. For the transgranular fracture, the crack often propagated across the lath and not along the block or packet boundary regardless of the test condition. On the other hand, the prior austenite grain boundary was the main path of hydrogen-related crack propagation when the test frequency was low.

Figure 8 shows high magnification (a) and (d) SEM images (backscattering electron images), (b) and (e) EBSD-

orientation maps, and (c) and (f) kernel average misorientation (KAM) maps obtained by EBSD (EBSD-KAM maps) around the fatigue cracks of the (a)–(c) uncharged and (d)–(f) hydrogen-charged specimens at  $f = 10$  Hz. The observation areas in both of the uncharged and hydrogen-charged specimens are  $1200 \mu\text{m}$  far from the side edges of the specimens. KAM represents the average misorientation degree around a measurement point. The present study used the orientation data of the nearest neighboring points around a measurement point to make the EBSD-KAM maps. As shown in the EBSD-orientation maps (Figs. 8(b) and 8(e)), the significant orientation change can be observed in the vicinity of the crack. Moreover, there are several (sub-)grains whose orientation is clearly different from the adjacent original martensite region. This could be because of

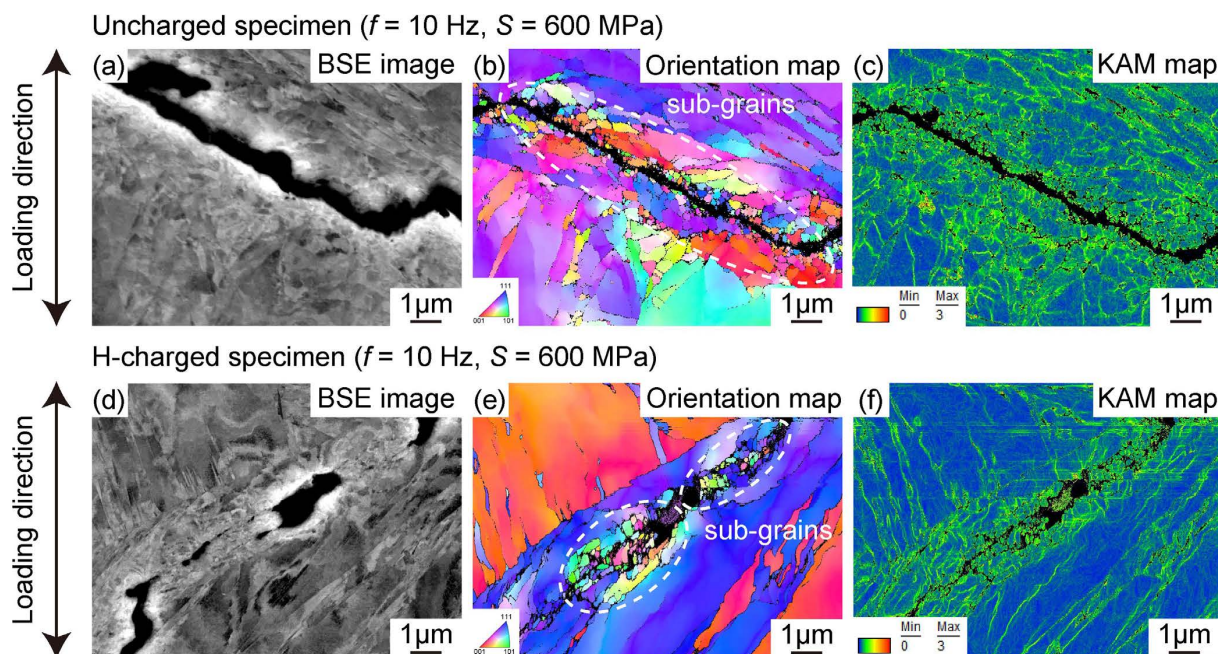


**Fig. 8.** (a) and (d) SEM-BSE images, (b) and (e) EBSD-orientation maps, and (c) and (f) EBSD-KAM maps showing the areas around the cracks of the (a)–(c) uncharged specimen ( $f = 10$  Hz,  $S = 600$  MPa) and (d)–(f) hydrogen-charged specimen ( $f = 10$  Hz,  $S = 600$  MPa). (Online version in color.)

high strain accompanying fatigue-crack propagation. The EBSD-KAM map shown in Fig. 8(c) indicates that the high-strained region exists over a relatively wide area (approximately  $2.15 \mu\text{m}$  from the crack) in the uncharged specimen. In the case of hydrogen-charged specimen (Fig. 8(f)), on the other hand, the high-strained region is limited only around the crack (approximately  $1.63 \mu\text{m}$  from the crack), indicating that the hydrogen-related fatigue-crack propagation was accompanied by intense localized plastic deformation.

#### 4. Discussion

It has been reported that, under hydrogen environment, fracture starts to occur by intergranular cracking on prior austenite grain boundaries in slow strain-rate tensile test,<sup>22)</sup> constant loading test,<sup>23)</sup> and fatigue test.<sup>20)</sup> Momotani *et al.*<sup>22)</sup> used hydrogen micro-print technique and reported that hydrogen accumulated on prior austenite grain boundaries during tensile test especially at low strain rate, leading to intergranular fracture. Assuming that most of the fatigue life were spent on crack initiation stage, the fatigue life would correspond to necessary condition to accumulate critical local hydrogen concentration at prior austenite grain boundaries. The results shown in Fig. 3 strongly support this idea. Although the test frequency affected the number of cycles to failure (*i.e.*, it decreased with decreasing test frequency), the total time to failure was independent of the test frequency. Previous studies<sup>22,24,25)</sup> reported that the degradation of tensile properties by hydrogen increased with decreasing strain rate. The decreasing strain rate corresponds to increasing the total period under deformation. Therefore, in conjunction with the fatigue test results in the present study, we can say that the period for accumulation of hydrogen (*i.e.*, diffusion behavior of hydrogen during deformation) is a very important parameter for susceptibility to hydrogen embrittlement. For crack propagation stage at the low test

frequency, we can consider that there was enough time for hydrogen to accumulate on prior austenite grain boundaries in the vicinity of crack tip in each fatigue cycle, leading to formation and coalescence of micro-cracks along prior austenite grain boundaries. On the other hand, in the case of high test frequency, the cracks successively propagated in transgranular manner before hydrogen accumulated on prior austenite grain boundaries in the vicinity of crack tip enough for inducing intergranular crack. These could be the reasons why the fraction of cracks propagated along the prior austenite grain boundaries increased with decreasing test frequency. In addition, the stress range affected the area fraction of intergranular surface in the hydrogen-charged specimen as well as the test frequency (Fig. 5). At low stress range, crack growth was slow, and there was enough time for hydrogen to accumulate on prior austenite grain boundaries in the vicinity of crack tip, resulting in increasing the fraction of intergranular fracture. Large plastic deformation, which led to formation of sub-grains, accompanied fatigue-crack propagation as shown in Fig. 8. However, the EBSD-KAM maps shown in Figs. 8(c) and 8(f) revealed that the plastic deformation was highly localized in the vicinity of the crack in the hydrogen-charged specimen. Ogawa *et al.* performed fatigue tests in a pure iron, and reported that acceleration of crack growth rate accompanied the reduction of plasticity expansion region due to the presence of hydrogen.<sup>26)</sup> Therefore, the high localization of plastic deformation observed in Figs. 8(d)–8(f) could lead to acceleration of crack growth. Based on the experimental results, we can suggest that the intergranular cracking and high localization of plastic deformation are the possible reasons for decreasing the fatigue life by the presence of hydrogen.

#### 5. Conclusions

The present study investigated the characteristics of

hydrogen-related fatigue fracture under various test frequencies in low-carbon martensitic steel. The major conclusions can be summarized as follows:

(1) The number of cycles to failure in the hydrogen-charged specimen was much smaller than that in the uncharged specimen. Moreover, the effect of hydrogen on the number of cycles to failure became prominent with decreasing test frequency. However, the time to failure was almost the same regardless of the test frequency in the hydrogen-charged specimen. The results suggest that the fatigue life would correspond to necessary condition to accumulate critical local hydrogen concentration at prior austenite grain boundaries for inducing intergranular cracking.



(2) The fracture surface of the uncharged specimen was mainly composed of transgranular surface, while that of the hydrogen-charged specimen was composed of transgranular surface and intergranular surface. In particular, the fraction of intergranular surface increased with decreasing test frequency. In the case of transgranular fracture, most of the cracks propagated across the laths in both of the uncharged and hydrogen-charged specimens regardless of the test frequency. The fraction of crack propagation along prior austenite grain boundaries increased with decreasing test frequency in the hydrogen-charged specimen.

(3) The high-strained region was confirmed over a relatively wide area in the uncharged specimen. On the other hand, the hydrogen-related fatigue-crack propagation was accompanied by intense localized plastic deformation, which could accelerate crack growth. The intergranular cracking and high localization of plastic deformation could be the possible reasons for decreasing the fatigue life by the presence of hydrogen.

### Acknowledgement

This study was financially supported by JSPS KAKENHI Grant Number JP19H02459, JP20K21083, JST “the establishment of university fellowships towards the creation of science technology innovation” Grant Number JPMJFS2123, the Elements Strategy Initiative for Structural Materials (ESISM) from MEXT Japan.

### ORCID

Akinobu SHIBATA  <https://orcid.org/0000-0001-8577-6411>  
Nobuhiro TSUJI  <https://orcid.org/0000-0002-2132-1327>

### REFERENCES

- 1) A. R. Marder and G. Krauss: *Trans. Am. Soc. Met.*, **60** (1967), 651.
- 2) G. Krauss and A. R. Marder: *Metall. Trans.*, **2** (1971), 2343.
- 3) S. Morito, H. Tanaka, R. Konishi, T. Furuhashi and T. Maki: *Acta Mater.*, **51** (2003), 1789. [https://doi.org/10.1016/S1359-6454\(02\)00577-3](https://doi.org/10.1016/S1359-6454(02)00577-3)
- 4) S. Morito, X. Huang, T. Furuhashi, T. Maki and N. Hansen: *Acta Mater.*, **54** (2006), 5323. <https://doi.org/10.1016/j.actamat.2006.07.009>
- 5) A. Shibata, T. Nagoshi, M. Sone, S. Morito and Y. Higo: *Mater. Sci. Eng. A*, **527** (2010), 7538. <https://doi.org/10.1016/j.msea.2010.08.026>
- 6) H. Ghassemi-Armaki, P. Chen, S. Bhat, S. Sadagopan, S. Kumar and A. Bower: *Acta Mater.*, **61** (2013), 3640. <https://doi.org/10.1016/j.actamat.2013.02.051>
- 7) Y. Mine, K. Hirashita, H. Takashima, M. Matsuda and K. Takashima: *Mater. Sci. Eng. A*, **560** (2013), 535. <https://doi.org/10.1016/j.msea.2012.09.099>
- 8) L. Morsdorf, O. Jeannin, D. Barbier, M. Mitsuhara, D. Raabe and C. C. Tasan: *Acta Mater.*, **121** (2016), 202. <https://doi.org/10.1016/j.actamat.2016.09.006>
- 9) K. Okada, A. Shibata, Y. Takeda and N. Tsuji: *Int. J. Fatigue*, **143** (2021), 105921. <https://doi.org/10.1016/j.ijfatigue.2020.105921>
- 10) S. Ueki, T. Matsumura, Y. Mine, S. Morito and K. Takashima: *Scr. Mater.*, **173** (2019), 80. <https://doi.org/10.1016/j.scriptamat.2019.08.004>
- 11) S. Ueki, Y. Mine and K. Takashima: *Mater. Sci. Eng. A*, **773** (2020), 138830. <https://doi.org/10.1016/j.msea.2019.138830>
- 12) S. Ueki, Y. Mine, X. Lu, Y. L. Chiu, P. Bowen and K. Takashima: *Scr. Mater.*, **203** (2021), 114045. <https://doi.org/10.1016/j.scriptamat.2021.114045>
- 13) H. J. Cialone and J. H. Holbrook: *Metall. Trans. A*, **16** (1985), 115. <https://doi.org/10.1007/BF02656719>
- 14) A. J. Slifka, E. S. Drexler, N. E. Nanninga, Y. S. Levy, J. D. McColskey, R. L. Amaro and A. E. Stevenson: *Corros. Sci.*, **78** (2014), 313. <https://doi.org/10.1016/j.corsci.2013.10.014>
- 15) Z. Sun, C. Moriconi, G. Benoit, D. Halm and G. Henaff: *Metall. Mater. Trans. A*, **44** (2013), 1320. <https://doi.org/10.1007/s11661-012-1133-5>
- 16) B. P. Somerday, P. Sofronis, K. A. Nibur, C. San Marchi and R. Kirchheim: *Acta Mater.*, **61** (2013), 6153. <https://doi.org/10.1016/j.actamat.2013.07.001>
- 17) Y. Murakami and S. Matsuoka: *Eng. Fract. Mech.*, **77** (2010), 1926. <https://doi.org/10.1016/j.engfracmech.2010.04.012>
- 18) N. Nanninga, A. Slifka, Y. Levy and C. White: *J. Res. Natl. Inst. Stand. Technol.*, **115** (2010), 437. <https://doi.org/10.6028/jres.115.030>
- 19) L. Briottet, I. Moro, M. Escot, J. Furtado, P. Bortot, G. M. Tamponi, J. Solin, G. Odemer, C. Blanc and E. Andrieu: *Int. J. Hydrog. Energy*, **40** (2015), 17021. <https://doi.org/10.1016/j.ijhydene.2015.05.080>
- 20) H. Matsumiya, A. Shibata, K. Okada and N. Tsuji: *Int. J. Hydrog. Energy*, **46** (2021), 37509. <https://doi.org/10.1016/j.ijhydene.2021.09.011>
- 21) H. Matsunaga, O. Takakuwa, J. Yamabe and S. Matsuoka: *Philos. Trans. R. Soc. A*, **375** (2017), 20160412. <https://doi.org/10.1098/rsta.2016.0412>
- 22) Y. Momotani, A. Shibata, D. Terada and N. Tsuji: *Int. J. Hydrog. Energy*, **42** (2017), 3371. <https://doi.org/10.1016/j.ijhydene.2016.09.188>
- 23) A. Shibata, Y. Takeda, Y. Kimura and N. Tsuji: *Metals*, **12** (2022), 440. <https://doi.org/10.3390/met12030440>
- 24) T. Chida, Y. Hagihara, E. Akiyama, K. Iwanaga, S. Takagi, M. Hayakawa, H. Ohishi, D. Hirakami and T. Tarui: *ISIJ Int.*, **56** (2016), 1268. <https://doi.org/10.2355/isijinternational.ISIJINT-2015-565>
- 25) K. Ogawa, Y. Matsumoto, H. Suzuki and K. Takai: *ISIJ Int.*, **59** (2019), 1705. <https://doi.org/10.2355/isijinternational.ISIJINT-2019-130>
- 26) Y. Ogawa, D. Birenis, H. Matsunaga, A. Thøgersen, Ø. Prytz, O. Takakuwa and J. Yamabe: *Scr. Mater.*, **140** (2017), 13. <https://doi.org/10.1016/j.scriptamat.2017.06.037>